Numerical simulations on the motion of a heavy sphere in upward Poiseuille flow

Lei Liu[a,b], Jianmin Yang[a,b], Haining Lu[a,b,*], Xinliang Tian[a,b], Wenyue Lu[a,b]

[a] *State Key Laboratory of Ocean Engineering, Shanghai Jiao Tong University, Shanghai, 200240, China*
[b] *Collaborative Innovation Center for Advanced Ship and Deep-Sea Exploration, Shanghai, 200240, China*

ABSTRACT

A "heavy" sphere moving in upward Poiseuille flow is numerically investigated using direct numerical simulations (DNS). The overset mesh and the moving computation domain are utilized for simulating the long-distance motion of the sphere. The path trajectory, slip velocity and radial equilibrium position of the "heavy" sphere are analyzed. The pressure and shear stress distributions on the sphere surface are presented. The hydrodynamic forces on the sphere are further discussed by constraining various degrees-of-freedom (DOFs) of sphere motion. The effects of tube Reynolds numbers (Re_t) and sphere-to-fluid density ratios (ρ_r) on the sphere motion are evaluated. As the increase of Re_t, five types of path trajectories of the sphere are observed at $\rho_r = 2$: helical falling, oscillating falling, vertical falling, vertical rising, and chaotic rising. The slip Reynolds number (Re_s) corresponding to the density ratio plays a crucial role in the dynamic responses of the sphere. Three types of path trajectories are revealed with the variation of ρ_r at $Re_t = 1106$: steady, periodic oscillating, and chaotic.

1. Introduction

Freely moving particles in pipe flows are commonly observed in industrial flows. Examples are ores in lifting pipes in deep sea mining and pulverized coal in conveying pipelines. The particle migration in tube flows is a classic issue in fluid mechanics, particularly in two-phase flow. In the 1960s, Segré and Silberberg (1961) discovered that the dilute suspended neutrally buoyant spheres in tube flows migrate away from both the wall and the centerline and accumulate at a radial position of approximately 0.6 times the tube radius, namely, the Segré–Silberberg effect. Numerous experimental and theoretical works have been conducted to verify and explain the particle migration in a tube (Jeffrey and Pearson, 1965; Karnis et al., 1966; Schonberg and Hinch, 1989; Asmolv, 1999). Comprehensive reviews of theoretical and experimental studies have been presented by Brenner (1966), Cox and Mason (1971), and Leal (1980) in early years.

As one of the simplest shear flows in tubes, the Poiseuille flow with velocity profile defined as $u = u_m(1 - (r/R)^2)$ (u_m is the maximum flow velocity in the tube center, r is the radial position, and R is the radius of the tube) has been widely considered in previous studies when investigating particle migration in tubes. Generally, the spherical particles have been selected. The tube Reynolds number $Re_t = u_m R/\nu$ (ν is the kinematic viscosity of the fluid) is one of the key factors affecting the particle motion and flow pattern in the tube. Analytical expressions

have already been provided by numerous researchers since the 1960s (Bretherton, 1962; Saffman, 1965; Asmolv, 1999); however, the results were mostly based on perturbing Stokes flow or potential flow, which limited the applications of the expressions. Feng et al. (1994) investigated the migration of a two-dimensional circular particle in Poiseuille flow at $Re_t \approx O(10)$ ($Re_{tmax} = 120$) by numerical simulations. Focusing on the axial and radial migration of the sphere and the lift force, four types of contributions to the lift force were distinguished: a wall repulsion owing to lubrication, an inertial lift related to shear slip, a lift owing to particle rotation, and a lift caused by the velocity profile curvature. Yu et al. (2004) analyzed the Saffman force (introduced by the fluid rotation $\nabla \times u$) and the Magnus force (related to the sphere rotation and the velocity difference between the sphere and the fluid) at $Re_t \approx 100$ and concluded that it was challenging to establish general formulae to measure lift forces by separately considering each of the effects described by Feng et al. (1994). The sphere migration at high tube Reynolds numbers $Re_t \approx 2000$ was investigated by experiments (Matas et al. (2003, 2004b,a), $Re_{tmax} = 2400$) and numerical simulations (Shao et al. (2008), $Re_{tmax} = 2200$). An inner equilibrium position of the particles was observed by Matas et al. (2004a) at $Re_t > 600$ when compared to the results of Segré and Silberberg (1961). The Segré–Silberberg effect disappears at $Re_t = 1500$ owing to the strong velocity fluctuations of the particles; the system is close to the laminar–turbulent transition at this Re_t (Matas et al., 2004b).

It is noteworthy that spheres are almost neutrally buoyant (Segré and Silberberg, 1961; Patankar et al., 2001; Schonberg and Hinch, 1989; Matas et al., 2004a; Shao et al., 2008) or marginally denser than the fluid (Jeffrey and Pearson, 1965; Hogg, 1994; Feng et al., 1994; Asmolv, 1999; Yu et al., 2004) when considering the sphere migration in Poiseuille flow. The maximum values of the density ratio between the sphere and fluid ρ_r (= ρ_s/ρ_f, where ρ_s is the particle density and ρ_f is the fluid density) were 1.1 and 1.05 in the studies of Feng et al. (1994) and Yu et al. (2004), respectively. The slip Reynolds number $Re_s = V_{slip}d/\nu$ (d is the sphere diameter, $V_{slip} = u_f - V_s$ is the slip velocity, where u_f is the undisturbed flow velocity in the position of the sphere center, V_s is the sphere velocity) is approximately $O(1)$ or less in previous studies.

In fact, "heavy" particles (we simply define "heavy" as the density ratio of $\rho_r \geq 1.1$) in upward pipe flows are commonly observed in engineering applications such as those of the pulverized coal ($\rho_r \approx 1.4$) in hydraulic transporting systems and the fine ores ($\rho_r \approx 2.0$) in vertical lifting systems during deep sea mining. The dynamic responses, including the path trajectory, slip velocity and radial equilibrium position, of a "heavy" particle at different Re_t are significant when selecting the pipe flow velocity to transport the particles. However, the density ratio considered in the previous studies was so small ($\rho_r \leq 1.1$) that the industrial applications of the obtained conclusions were limited. Although the role of density ratio on the sphere migration has been evaluated in quiescent fluid (Jenny et al., 2004; Horowitz and Williamson, 2010; Namkoong et al., 2008; Deloze et al., 2012; Zhou and Dušek, 2015), the results cannot be applied directly to the cases of the upward pipe flow. Consequently, a detailed analysis of the migration of "heavy" spheres in vertical Poiseuille flow is required; the effects of Re_t and ρ_r on sphere migration and flow pattern need to be evaluated.

In this paper, the motion of a "heavy" sphere in Poiseuille flow is investigated using direct numerical simulation (DNS) method. The overset mesh and the moving computational domain are applied to model the long-distance motion of the sphere. The influences of Re_t on the path trajectory of the sphere and the surrounding wake structures are evaluated at $0 \leq Re_t \leq 1998$. The density ratio ρ_r varies in the range of $1.1 \leq \rho_r \leq 4$, which covers most of the particle densities in engineering applications. The corresponding slip Reynolds number is $Re_s \approx O(10^2)$, which is larger than that in the literature ($O(1)$ and $O(10)$).

The remainder of this paper is organized as follows. The mathematical formulae are provided in Section 2. The computational overview and validation studies are presented in Section 3. The results and discussion are described in Section 4. Finally, the concluding remarks are presented in Section 5.

2. Mathematical formulae

Incompressible flow is governed by the Navier–Stokes (N–S) equations expressed as follows:

$$\nabla \cdot \boldsymbol{u} = 0 \tag{1}$$

$$\frac{\partial \boldsymbol{u}}{\partial t} + \boldsymbol{u} \cdot \nabla \boldsymbol{u} = -\frac{1}{\rho_f}\nabla p + \nu \nabla^2 \boldsymbol{u} + \boldsymbol{f_g} \tag{2}$$

where $\boldsymbol{u}$ is the velocity of the fluid, p represents the pressure, $\boldsymbol{f_g}$ denotes the gravitational force, ρ_f labels the density of the fluid, ν is the kinematic viscosity, and t is the time.

The N–S equations are discretized using the finite volume method (FVM). The discretization of each term is formulated by integrating the term over a control volume using Gauss's theorem. Here, the second-order upwind scheme is used to discretize the convective term; the implicit unsteady solver is applied to carry out the transient computation; the second-order temporal discretization is utilized to obtain more accurate results compared to the first-order temporal discretization. For each time step, the SIMPLE (Semi-Implicit Method for Pressure-Linked

Equation) scheme is adopted to solve the governing equations for the velocity component and the pressure-correction equation.

The six-degree-of-freedom (6DOF) motion solver is employed to simulate the sphere migration in response to the flow-induced forces and gravity. First, the resultant forces acting on the sphere are calculated and are used to solve the governing equations of sphere motion:

$$m\frac{d\boldsymbol{V}}{dt} = \boldsymbol{F} \tag{3}$$

$$A\frac{d\boldsymbol{\omega}}{dt} + \boldsymbol{\omega} \times A\boldsymbol{\omega} = \boldsymbol{M} \tag{4}$$

where m represents the sphere mass, $\boldsymbol{V}$ demotes the velocity of the sphere center, A is the tensor of the moments of inertia, and $\boldsymbol{\omega}$ is the angular velocity of the sphere. $\boldsymbol{F}$ and $\boldsymbol{M}$ are the resultant force and moment, respectively, on the sphere.

In this study, the dimensionless forms of the calculated results are used. The reference scales used to non-dimensionalize the results are as follows: $L_0 = d$ for length, $V_0 = \sqrt{(\rho_r - 1)gd}$ for velocity, $\omega_0 = \sqrt{(\rho_r - 1)g/d}$ for angular velocity, $T_0 = \sqrt{d/((\rho_r - 1)g)}$ for time, $F_0 = \rho_f g\pi d^3/6$ for force and $M_0 = \rho_f g\pi d^4/6$ for moment.

3. Computational overview and validation study

3.1. Computational overview

A sphere moving in upward Poiseuille flow inside a vertical circular tube is considered here. The sphere is impelled under gravitational and hydrodynamic forces. Fig. 1 shows the computational domain and the boundary conditions in the present study. The diameters of the sphere and circular tube are d and D, respectively. The diameter ratio between the tube and sphere D/d is set as 4. The numerical simulations are
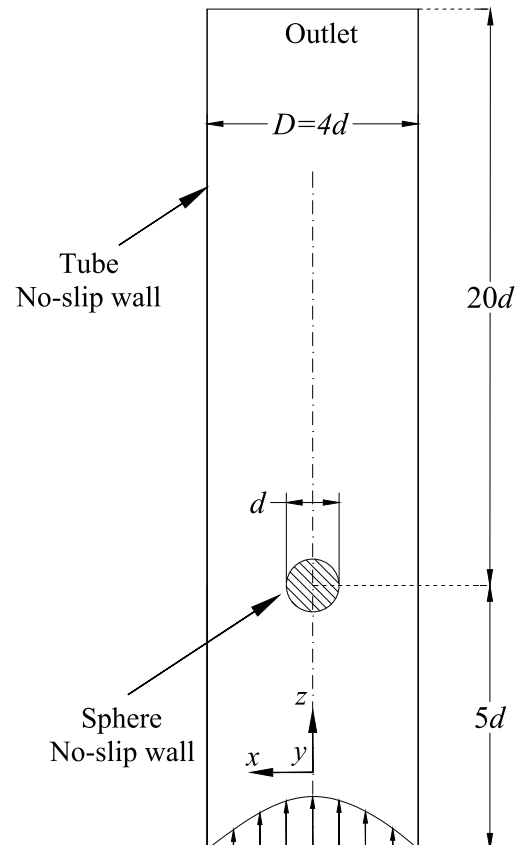

Fig. 1. (x, z)-plane view of computational domain and boundary conditions.

conducted by using the CFD code StarCCM + V11.06, which has been widely used to simulate moving objects in the literature (Romero-Gomez and Richmond, 2016; Liang and Tao, 2017; Liu et al., 2017; Chandar et al., 2018).

At the inlet boundary, the Poiseuille flow, $u = u_m(1 - (r/R)^2)$ is prescribed (Yang et al., 2005; Jiang et al., 2013). At the outlet boundary, the pressure is set to zero, and the velocity is specified as a zero normal gradient. On the sphere surface, the velocity is set as zero to represent the no-slip wall condition, and the pressure is set as a zero normal gradient. On the tube wall, a no-slip wall boundary condition is applied. The initial condition of the flow inside the tube is set as Poiseuille flow: $u = u_m(1 - (r/R)^2)$. It has been verified that the effects of the boundary on the calculated results are negligible.

Rather than constructing a long computational domain, a moving computational domain is used to model the long-distance and long-time motion of the sphere in the upward flow (Asao et al., 2013; Rahmani and Wachs, 2014). The computational domain is set as moving vertically at a vertical velocity the same as that of the sphere. The wall tangential velocity relative to the computational domain is set as the same value, albeit in the opposite direction, to cancel out the additional velocity and acceleration caused by the moving computational domain. Owing to the fact that the velocity and acceleration of computational domain are only exerted on the wall boundary rather than each volume cell in the computational domain, no additional velocity would be superposed on the Poiseuille flow (CD-adapco, 2016). Therefore, the moving computational domain can be used to simulate the Poiseuille flow in an infinitely long tube. Before conducting the simulations of the sphere migration, the Poiseuille flow has been validated without the sphere.

In order to address the rotation and large-amplitude horizontal migration of the sphere, we adopt the overset mesh scheme which has been widely used for simulating the free-fall of cylinders (Romero-Gomez and Richmond, 2016) and spheres (Deloze et al., 2012; Koblitz et al., 2017) in the published works. Conceptually, the computational domain is discretized into several different meshes that overlap each other; the characteristics, including the shape and the motion, of the meshes are different. This feature is useful in problems dealing with large-amplitude movement of objects. At each time step, the meshes do not have to be regenerated or modified, thus offering greater flexibility over other mesh techniques such as mesh morphing (CD-adapco, 2016). Additionally, local grid refinements on the particle surfaces contribute to capturing the viscous boundary layer accurately without appreciably increasing the total grid point count, thereby saving the computational costs when compared to the static grid methods (Koblitz et al., 2017).

In the present study, two sets of meshes are generated: a spherical overset mesh containing the moving sphere and a cylindrical background mesh enclosing the entire domain, as shown in Fig. 2 (a). Considering the sphere diameter d, the tube diameter D, the thickness of boundary layers and the grid resolution near the sphere, the spherical

overset mesh is designed with a diameter of $3.3d$; the center of the overset mesh coincides with the sphere center. The overset mesh is overlaid on the background mesh with the outer boundary defined as the overset condition to separate the background mesh into an active part (the blue mesh) and an inactive part (covered by the red overset mesh). The flow will be computed in the overset mesh and the active part of the background mesh, almost similar to a continuous mesh. The flow solutions at the interface (overlapping cells, the greens cells in Fig. 2(a)) are obtained from the interpolation of both the overset and background meshes, rather than solving the governing equations directly, to establish the connectivity between the meshes.

Fig. 2(b) shows the algorithm in the overlapping cells. The background mesh is in blue, whereas the overset mesh is in red. Two main aspects are considered: the flow quantities at the last active overset cell (C in Fig. 2(b)) and the fluxes through the cell face between C and A (the "acceptor" cell marked by a red hollow circle in Fig. 2(b)). A two-step overset process is conducted. Firstly, the hole cutting step is conducted to estimate the cells that take part in the flow field calculation. Secondly, the donor search is executed to determine the donor cells (N4, N5 and N6) contributing to the acceptor cells (A in Fig. 2(b)). The flow quantities at the acceptor cell A (ϕ_A) are calculated as $\phi_A = \sum \alpha_i \phi_{N_i}$, where α_i is the interpolation weighting factors and ϕ_{N_i} is the flow quantities at donor cells. The flow quantities at C are computed based on the usual algebraic representation of the governing equations, and involve three neighbor cells from the overset mesh (N1, N2 and N3) and three cells from the background mesh (N4, N5 and N6). The fluxes through the cell face between C and A are computed in a manner similar as for two active cells. More detailed descriptions of the overset mesh scheme are available in the literature (CD-adapco, 2016; Hadzic, 2006; Koblitz et al., 2017).

In our simulation, the computational domain is separated into sets of unstructured trimmed cells. A cutaway view of the grid structures is shown in Fig. 3(a). The grids are initially generated with a base size; refinements are applied in the zones containing the sphere and the surrounding vortices. The prism layer cells (CD-adapco, 2016) are used in the vicinity of the spheres and the pipe wall to capture further details of the flow in the boundary layers. In the present study, the convective Courant number is a maximum of 0.5 in most areas of the computational domain. At the beginning of the simulations, the sphere is fixed until the flow in the tube is fully developed.

3.2. Validation study

Validations of the spatial and temporal resolutions are conducted by evaluating the sedimentation of a sphere in quiescent fluid inside a vertical tube. The density ratio $\rho_r = 2$ is selected; the slip Reynolds number Re_s is approximately 263. Once the sphere is released, it accelerates rapidly (transit state) and finally moves helically (fully developed state), as shown in Fig. 7(a). Both the transit state and the fully
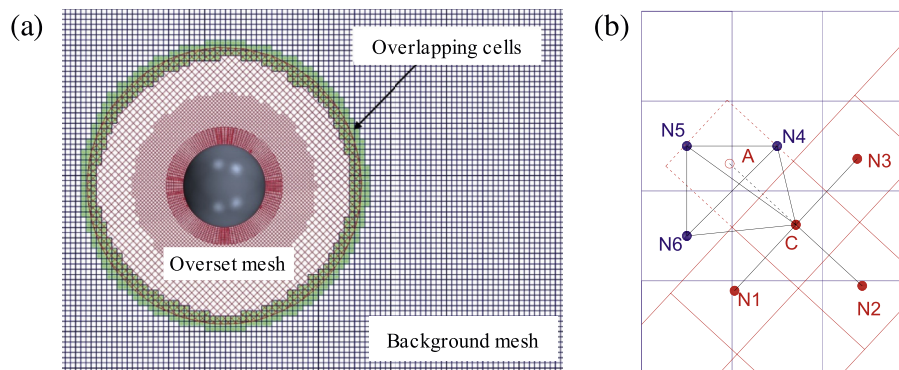

Fig. 2. The overset mesh. (a) A cutaway view of the overset mesh and (b) the interpolation scheme.
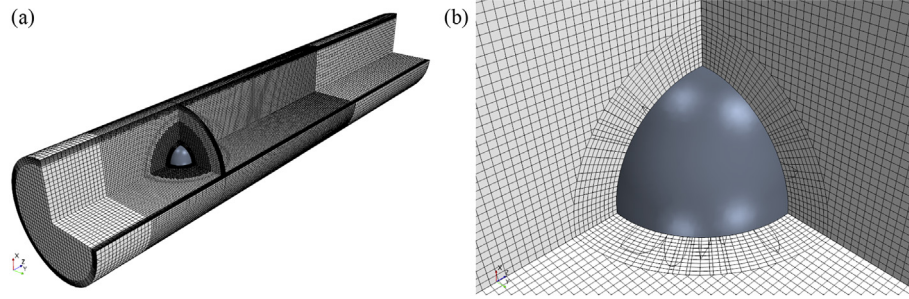
Fig. 3. Cutaway view of grid structures. (a) A general view and (b) grids around the sphere.

Table 1
Results of sphere motion with different meshes.

Case	Elements	$\Delta t/t_0$	X_h/R	V_z	V_h
A1	330,222	1/50	0.445	−1.2922	0.1275
A2	670,369	1/50	0.428	−1.2877	0.1206
A3	1,289,171	1/50	0.426	−1.2865	0.1174
A4	2,356,557	1/50	0.425	−1.2874	0.1166

Table 2
Results of sphere motion with different time-step sizes.

Case	Elements	$\Delta t/t_0$	X_h/R	V_z	V_h
B1	1,289,171	1/10	0.446	−1.2836	0.1152
B2	1,289,171	1/25	0.435	−1.2853	0.1177
B3(A3)	1,289,171	1/50	0.426	−1.2865	0.1174
B4	1,289,171	1/100	0.423	−1.2865	0.1174

developed state of the sphere motion have been compared at four meshes (Cases A1~A4) and four time-step sizes (Cases B1~B4). The average values of the radial position X_h/R, vertical velocity V_z and the

magnitude of horizontal velocity V_h of the sphere in the fully developed states are summarized in Table 1 and Table 2. The time histories of the sphere velocities, V_z and V_h, in the transit states are compared in Fig. 4.

As shown in Table 1, a reasonable convergence is observed in the results of X_h/R, V_z and V_h in the fully developed states as the increase of mesh elements. Moreover, the time histories of V_z and V_h in Cases A3 and A4 match adequately in the transit states, as illustrated in Fig. 4(a) and (c), respectively. When focusing on the time-step size, highly marginal differences exist in the results in Cases B3(A3) and B4, both in the transit states (see Fig. 4(b) and (d)) and in the fully developed states (see Table 2). Therefore, based on the validations above, the spatial resolution in Case A3 and the time-step size of $\Delta t/t_0 = 1/50$ will be used in the following simulations.

To verify the capability of our numerical method, we simulate the sedimentation of a sphere in a vertical tube and compare the calculated sphere migration to the DNS results of Deloze et al. (2012). The initial configuration of our simulations is the same as that of Deloze et al. (2012). The vertical velocity V_z at $Re_s = 189$ (the corresponding Galileo number $G = 150$, which is defined as $G = \sqrt{(\rho_r - 1)gd^3}/\nu$ (Deloze et al., 2012)) and the horizontal velocity V_x at $Re_s = 213$ ($G = 165$) are revealed in Fig. 5(a) and Fig. 5(b), respectively. The time histories of both
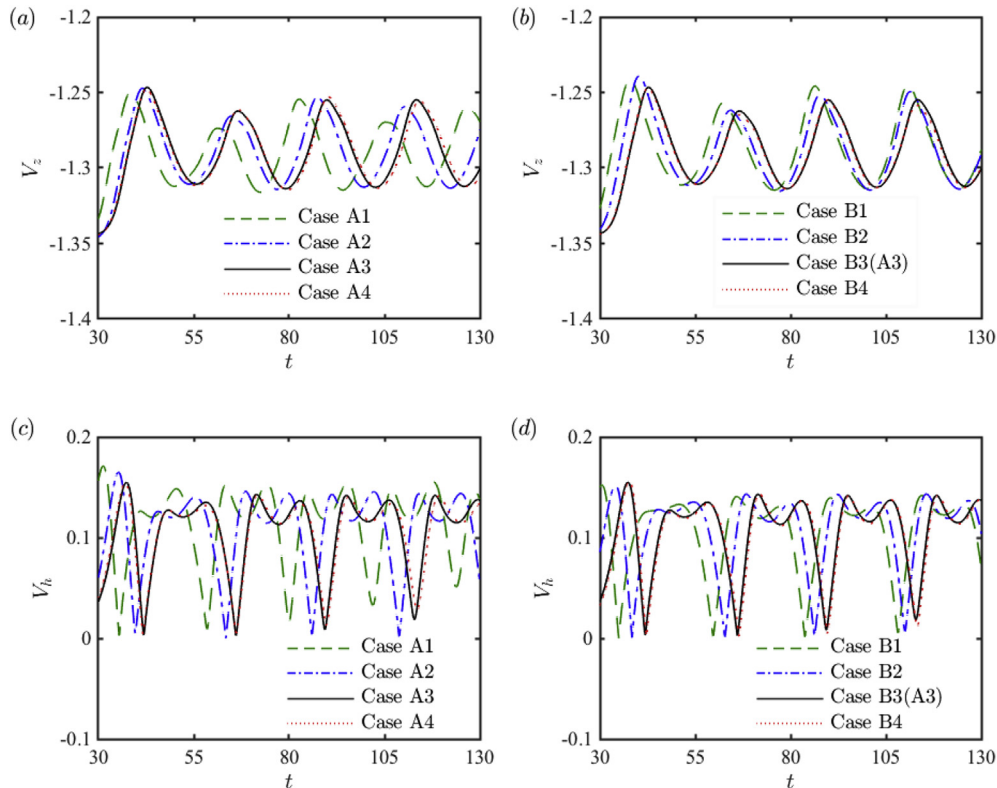

Fig. 4. Time histories of sphere velocities in the transit states. (a) and (c) V_z and V_h at different mesh resolutions; (b) and (d) V_z and V_h at different time-step sizes.
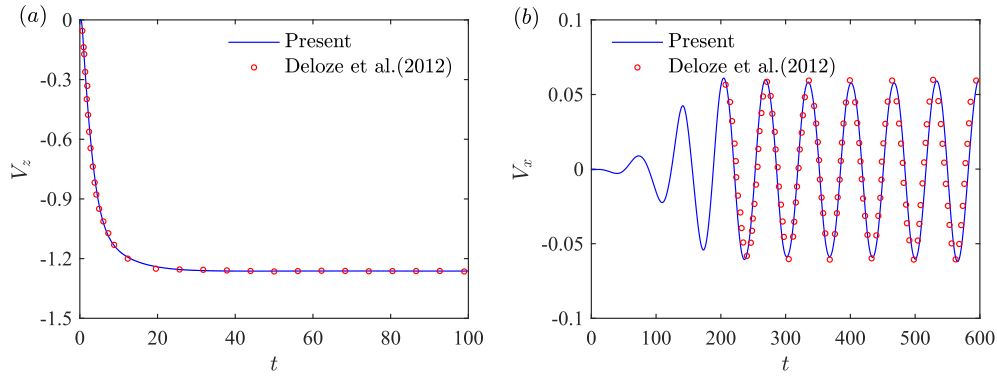
Fig. 5. Comparison of (a) V_z at $G = 150$ and (b) V_x at $G = 165$ to DNS results of Deloze et al. (2012).
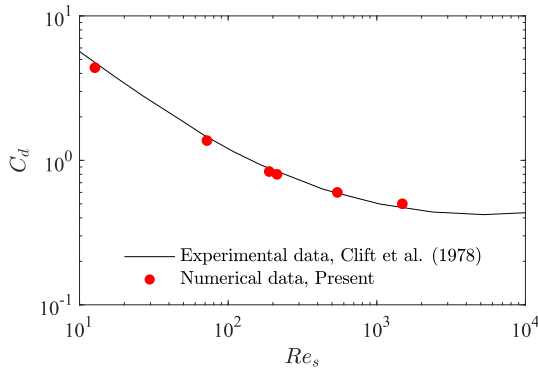

Fig. 6. Comparison of present numerical results to experimental results of Clift et al. (1978).

V_z and V_x exhibit favorable agreement with the DNS data of Deloze et al. (2012). In addition, the calculated drag coefficients C_d $\left(= F_z / \left(\frac{1}{8}\rho_f V_z^2 \pi d^2\right)\right)$ of freely falling spheres in a vertical tube has been compared to the experimental data of Clift et al. (1978) at different Re_s, as shown in Fig. 6. Marginal differences can be distinguished from the numerical and experimental data. From these two validation cases, we conclude that the present numerical method is valid for simulating the sphere migration in a vertical tube.

4. Results and discussion

4.1. Sphere migration at different Re_t

The tube Reynolds number Re_t is one of the key parameters dominating the motion of a "heavy" sphere. Different path trajectories are observed in upward Poiseuille flows at different Re_t. This section describes a series of numerical simulations conducted at $Re_t \leq 1998$. The typical density ratio $\rho_r = 2$ is selected. The corresponding u_m is in the range of $0 \leq u_m \leq 4.9$ in the present study.

4.1.1. Five types of path trajectories

As shown in Fig. 7, five types of path trajectories can be observed at different Re_t: helical falling, oscillating falling, vertical falling, vertical rising, and chaotic rising.

The instantaneous wake structures in the asymptotic states of the sphere motion are presented in Fig. 8. The vortical structures are identified by the isosurface of the Q-criterion proposed by Hunt et al. (1988):

$$Q = -\frac{1}{2}(\|\mathbf{\Omega}\|^2 - \|\mathbf{S}\|^2) \tag{5}$$

where $\mathbf{S}$ and $\mathbf{\Omega}$ denote the strain and rotation tensors, respectively. The Q-criterion has been widely used to represent the three-dimensional vortical structures (Tian et al., 2017a, b). In addition, Fig. 9 shows the streamlines of the flow in the longitudinal section (crossing the tube centerline and sphere center) of the computational domain. Here, the velocity field is relative to the moving reference frame of the sphere.

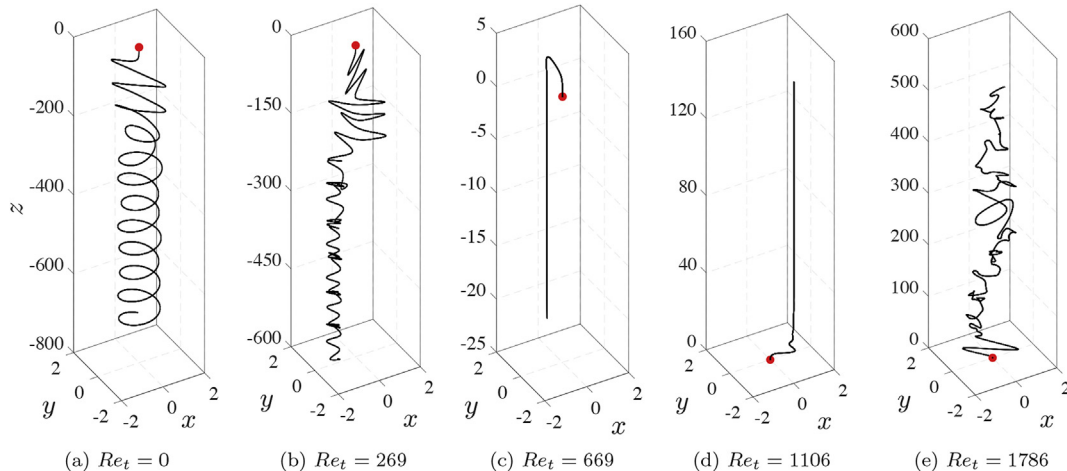First, we consider the helical fall of a "heavy" sphere in quiescent

Fig. 7. Trajectories of sphere at different Re_t in Poiseuille flow. The red points represent the initial positions of spheres. (For interpretation of the references to colour in this figure legend, the reader is referred to the Web version of this article.)
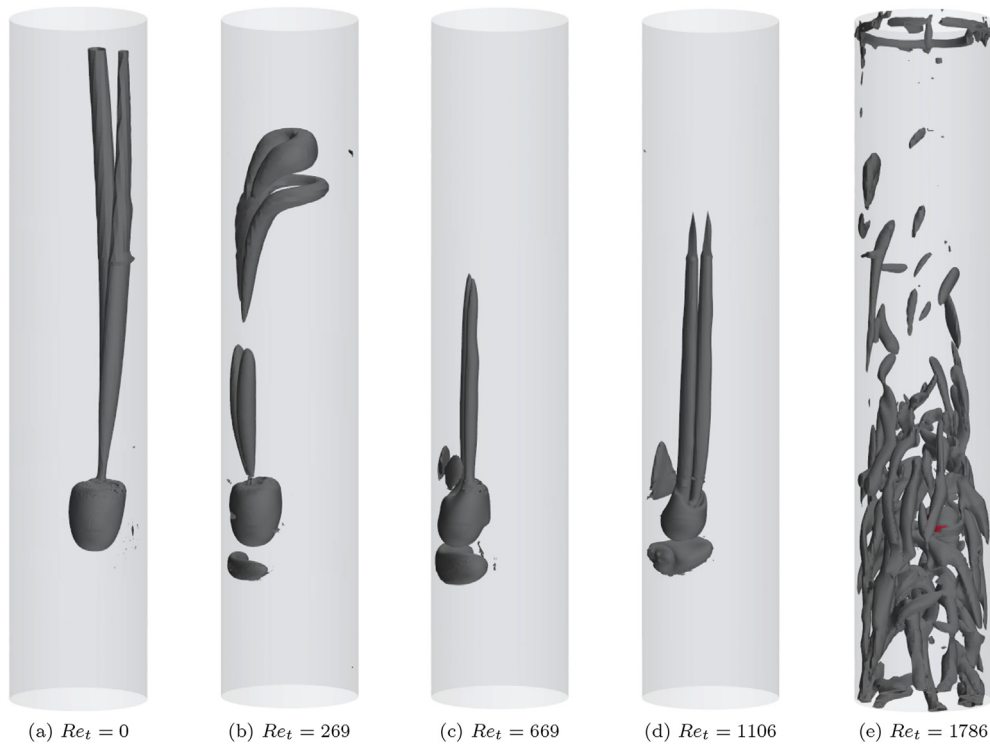
(a) $Re_t = 0$ (b) $Re_t = 269$ (c) $Re_t = 669$ (d) $Re_t = 1106$ (e) $Re_t = 1786$

Fig. 8. Vortical structures in the tube (identified by the iso-surfaces of Q). The red spot in (e) is the geometry of the sphere; it is covered by the vortex structures in (a)~(d). (For interpretation of the references to colour in this figure legend, the reader is referred to the Web version of this article.)

fluid ($Re_t = 0$) in a tube, as shown in Fig. 7(a). The slip Reynolds number is $Re_s = 263$ ($G = 203$). Once the sphere is released, the Hopf bifurcation breaks the original axisymmetry of the vertical fall (Deloze et al., 2012). The instability gives rise to the helical mode, and the surrounding flow results in non-zero lift on the sphere, leading to the helical trajectories of the sphere. In the asymptotic state of the helical fall, double-threaded wake structures are revealed in Fig. 8(a). The wake near the sphere is approximately planar symmetric, which can be reflected in the streamlines near the sphere (see Fig. 9(a)). The twist of the wake far from the sphere is due to the helical trajectory. From the viewpoint of both the trajectories and the wake structures, the helical fall in the tube is similar to the steady oblique state of an unconfined freely falling sphere (Jenny et al., 2004; Deloze et al., 2012). However, the oscillations due to the vortex shedding are observed around the mean oblique trajectory when the sphere is released in the unbounded fluid at $G = 203$ and $\rho_r = 2$ in the works of Jenny et al. (2004). The

different trajectories indicate that the tube wall has a tendency to suppress vortex shedding behind the sphere. Incidentally, the sphere trajectory in the tube is not always helical. It is determined by the density ratio ρ_r, diameter ratio D/d, and Galileo number G (Deloze et al., 2012).

The helical trajectory of the sphere has been broken by the Poiseuille flow in the tube. Following the analysis of Feng et al. (1994), the mechanisms responsible for the horizontal motion of the sphere are identified as follows: a lift caused by the shear flow (including the curvature of the velocity profile), the Magnus force associated with sphere rotation, the wall repulsion, and a lift force related to Re_s. Notably, the effect of Re_s has not been proposed by Feng et al. (1994) and Yu et al. (2004) owing to the small Re_s (approximately $O(1)$ in their works), at which no lift force would exist if there is no shear in the flow. However, a lift will be induced by the surrounding flow when $Re_s \geq 211$ even if the sphere is exposed to the homogeneous flow
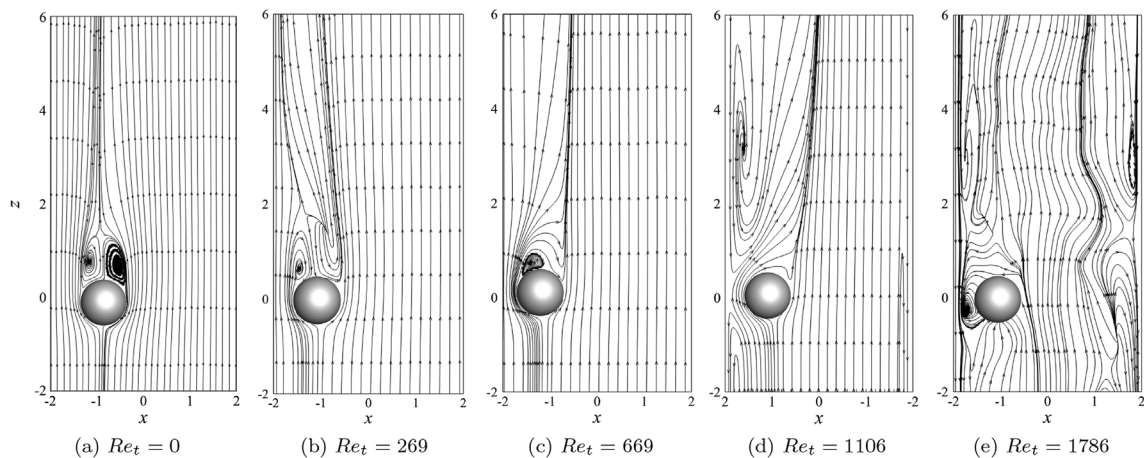

(a) $Re_t = 0$ (b) $Re_t = 269$ (c) $Re_t = 669$ (d) $Re_t = 1106$ (e) $Re_t = 1786$

Fig. 9. Streamlines of the flow (relative to sphere, in the longitudinal section) at different Re_t.

(Johnson and Patel, 1999). Therefore, the lift resulted from the Re_s should be considered when the slip Reynolds number is large ($Re_s \approx 263$ in the present study) in the cases of "heavy" spheres.

The sphere falls near the tube wall with horizontal oscillations at $Re_t = 269$ ($u_m = 0.66$), as shown in Fig. 7(b). An explanation for the oscillations is that the lift owing to the shear breaks the helical state of a freely falling sphere, however, can never achieve a static equilibrium with the effects of the sphere rotation, the wall repulsion and Re_s. As shown in Fig. 9(b), the flow field on both sides of the sphere in the longitudinal section is asymmetric; vortex shedding can be observed behind the sphere (Fig. 8(b)). When the vortices shed from the sphere, the fluctuations of the lift force are induced, leading to horizontal oscillations of the sphere.

As the increase of the tube Reynolds number ($Re_t = 669$ and 1106, the corresponding flow velocities are $u_m = 1.64$ and 2.72), a stable state of the sphere motion corresponding to an equilibrium of lift force can be obtained. The sphere moves vertically in the vicinity of the tube wall, as shown in Fig. 7(c) and (d). When compared to the unstable state at $Re_t = 269$, a remarkable effect of the shear on the lift is revealed at a higher Re_t. The shear adjusts the radial position and the rotation of the sphere, thus altering the wall repulsion and the Magnus force accordingly. The fluctuations of lift gradually vanish, leading to a stable state finally. Fig. 8(c) and (d) show the wake structures in the vicinity of the sphere and tube wall in the asymptotic state. Constant double-threaded structures of the flow can be observed behind the sphere. In addition, an annular structure and a pair of wing-like structures appear in the front and back, respectively, of the sphere when flow passes through the gap between the sphere and the wall, indicating the repulsive effect of the wall on the sphere.

As the flow velocity increases continuously ($Re_t = 1786$, $u_m = 4.38$), the path trajectory becomes chaotic (Fig. 7(e)). Owing to the tube Reynolds number close to the laminar–turbulent transition, the flow pattern would be affected strongly by a slight disturbance (Matas et al., 2003). Here, the sphere blocks the flow in the tube, resulting in the chaotic flow field (Figs. 8(e) and Fig. 9(e)). The sphere is impelled by the chaotic flow in return and moves irregularly.

4.1.2. Pressure and shear stress distributions

In a specific interval of Re_t, the sphere moves vertically. As the flow velocity increases, the falling velocity of the sphere decreases gradually, and the sphere is finally lifted. In this section, we focus on the pressure coefficient C_p (Fig. 10) and shear stress τ (Fig. 11) on the vertically moving spheres in the fully developed states. The vertical and horizontal projections of the pressure coefficient on the sphere surface are represented by C_{pz} and C_{ph}, respectively. τ_z and τ_h denote the vertical and horizontal components, respectively, of the shear stress. Following the work of Feng et al. (1994), the pressure and shear stress have been non-dimensionalized by $\frac{1}{2}\rho_f u_m^2$.

Generally, the pressure and shear stress act mainly on the upstream surface of the sphere ($90° < \theta < 270°$), as shown in Figs. 10 and 11. The pressure is approximately $4 \sim 6$ times the shear stress. This is related to

the slip Reynolds number ($Re_s \approx 263$), at which the shear stress is significant. As the flow velocity increases in the tube, the non-dimensional C_p and τ decrease.

Fig. 10(a) reveals that the maximum pressure coefficient appears at $190° \leq \theta \leq 200°$. The position where the maximum C_p appears is regarded as the stagnation point, which is slightly shifted backward on the sphere surface as the flow velocity increases. The shift of the stagnation point is mainly related to the shear of Poiseuille flow. The increase of Re_t changes the shear; the lift owing to the shear impels the sphere to a new equilibrium position. The sphere rotation is modified, and the wall-wake interaction is adjusted. Therefore, the flow in the layers that adhere to the sphere surface is influenced, resulting in the modification of the distributions of C_p and τ and the shift of the stagnation point.

As shown in Fig. 10(b), four apparent extreme points of C_{ph} can be observed on the falling sphere surface (at $Re_t = 555$ and 669). The two extrema close to the tube centerline ($180° < \theta < 360°$) are larger than those close to the tube wall ($0° < \theta < 180°$), indicating that the "intensity" of the flow in the gap between the sphere and the wall is weaker. The flow would pass through the gap "smoothly". This phenomenon is more conspicuous at larger Re_t: the extrema close to the wall almost disappear at $Re_t = 1106$ and 1207. It is noted that the phenomenon is inconsistent with the results of Feng et al. (1994). A possible explanation for the difference is the much larger slip Reynolds number ($Re_s \approx 263$ in the present study), at which the wake structures around the sphere are asymmetric even in the infinite homogeneous flow.

Fig. 11(a) and (b) show the vertical (τ_z) and horizontal (τ_h) components, respectively, of the shear stress on the sphere. The shear stress is mainly experienced on the upstream surface of the sphere ($90° < \theta < 270°$). Similar to the shift of stagnation point, the extreme points of τ_z and τ_h on the sphere are altered at different Re_t due to the change of the shear of Poiseuille flow. Two extrema of τ_z are observed in Fig. 11(a). The vertical shear stress τ_z on the side close to the wall is smaller than that on the side in the vicinity of the tube centerline, reflecting the weaker flow intensity in the gap between the sphere and the wall once again. Although the extrema of τ_h on both sides of the sphere are approximate, the distribution of τ_h is asymmetric since the stagnation point is on the side near the tube centerline.

4.1.3. Slip velocity and radial equilibrium position

The slip velocity and radial equilibrium position of a "heavy" sphere in Poiseuille flow are of more engineering interests when transporting the particles in pipelines. Fig. 12 and Fig. 13 show the slip velocity V_{slip} and the equilibrium position X_h/R, respectively, of the sphere at different u_m. Here, we use the flow velocity u_m rather than Re_t to provide an intuitive comparison between the slip velocity, the sphere velocity and the flow velocity. When referred to the helical and the oscillating trajectories (see Fig. 7(a) and (b)), the average radial positions of the sphere in the fully developed states are presented. The chaotic states of the spheres are excluded. In addition, the V_{slip} and X_h/R at $\rho_r = 1.8$ and
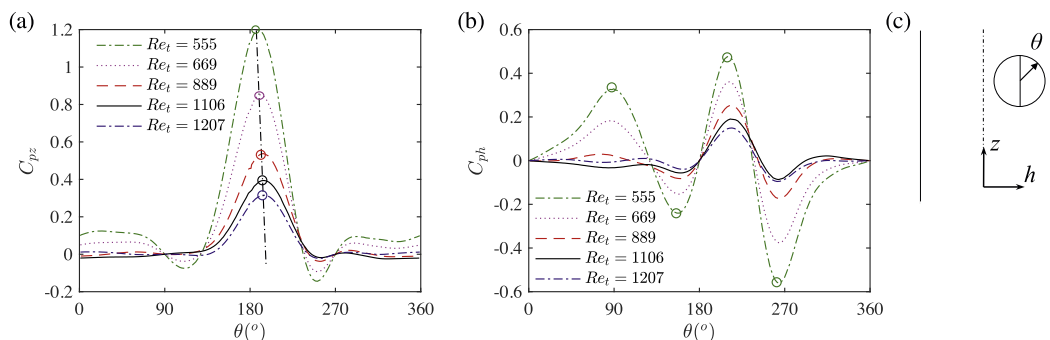

Fig. 10. Pressure coefficient distributions on sphere surface (in the longitudinal section).(a) Vertical projection C_{pz} and (b) horizontal projection C_{ph}.
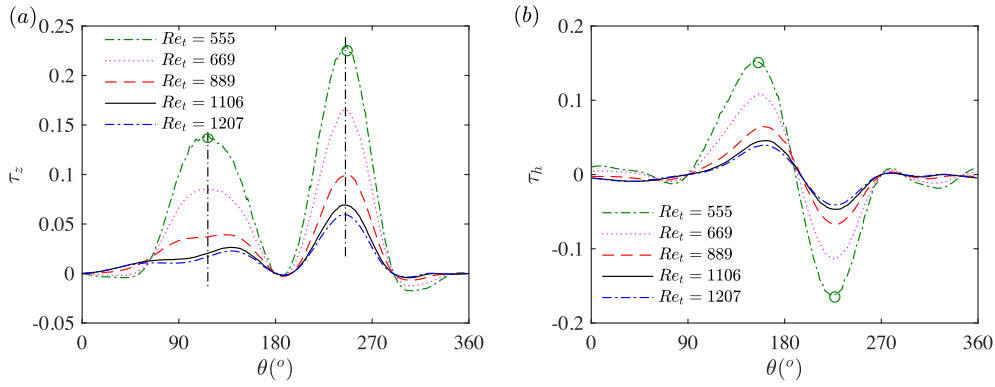
Fig. 11. Wall shear stress distributions on sphere surface (in the longitudinal section) (a) Vertical component τ_z and (b) horizontal component.τ_h
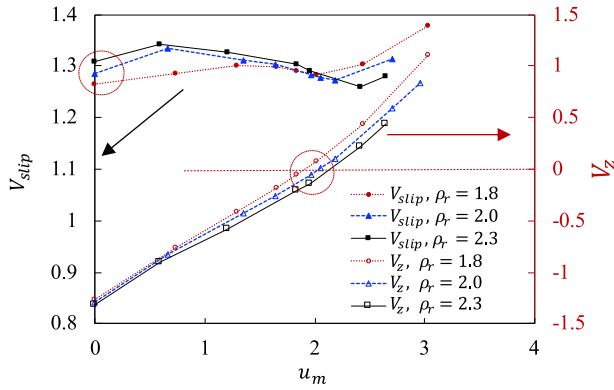

Fig. 12. Slip velocity V_{slip} and vertical velocity V_z of sphere.
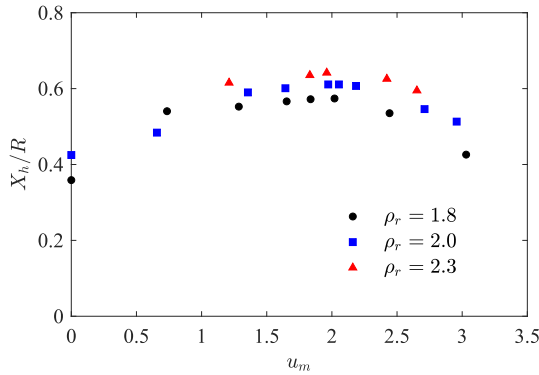

Fig. 13. Radial equilibrium position X_h/R of sphere.

2.3 are provided as a supplement to the results at $\rho_r = 2$.

As shown in Fig. 12, the trends of V_{slip} and V_z are similar at $\rho_r = 1.8$, 2.0, and 2.3. The slip velocity of the sphere in Poiseuille flow varies in a relatively small interval when u_m varies from 0 to 2.96 ($Re_t \leq 1207$, before the sphere trajectory becomes chaotic). The terminal velocity of the settling sphere in quiescent fluid is $V_{slip} \approx 1.3$, whereas the critical flow velocity which keeps the sphere suspending in the fluid, namely, the suspending velocity, is $u_m \approx 2$. That is to say, the sphere will not be lifted by Poiseuille flow until u_m is much larger than the terminal velocity of the sphere. However, the conclusion is qualitative, and a quantitative relation between the critical flow velocity and ρ_r is still required.

As revealed in Fig. 13, the equilibrium position of the sphere varies in a wide range of $0.4 \leq X_h/R \leq 0.66$, which is close to the results in the cases of neutrally ($X_h/R \approx 0.6$, Segré and Silberberg (1961)) and slightly non-neutrally buoyant spheres (Matas et al., 2004a; Jeffrey and Pearson, 1965; Feng et al., 1994). However, the effects of the shear, the

sphere rotation and the wall on the "heavy" sphere are likely to be different from those discussed in the literature (Feng et al., 1994). As the flow velocity increases, X_h/R increases to a maximum value (the sphere is closest to the wall) and then begins to decrease. The maximum equilibrium position appears at $u_m \approx 2$, which corresponds to the suspending velocity.

In summary, Re_t is one of the dominating parameters determining the path trajectory of a "heavy" sphere in Poiseuille flow. As the increase of Re_t, five types of path trajectories can be observed: helical falling, oscillating falling, vertical falling, vertical rising, and chaotic rising. The shear of Poiseuille flow plays an essential role in the final state of the lift force and the sphere motion. The slip velocity V_{slip} varies in a marginal interval at a constant ρ_r. The equilibrium radial position of the sphere is in a range of $0.4 \leq X_h/R \leq 0.66$ at different Re_t. The critical flow velocity to lift the sphere is larger than the terminal velocity of the sphere.

4.2. Hydrodynamic forces

The sphere migration is determined by the hydrodynamic forces of the flow; however, it affects the surrounding flow in return. The lift force and lateral migration of a non-neutrally buoyant sphere have been summarized by Feng et al. (1994) and Yu et al. (2004), however, at small slip Reynolds numbers ($Re_s \approx O(1)$). As Re_s is increased to $O(10^2)$, the principles of these factors are likely to be different.

In this section, the constrained numerical simulations, in which various DOFs of sphere motion are limited, are conducted to investigate the effects of the rotation and translation of a "heavy" sphere on the hydrodynamic forces. In the simulations, the density ratio is $\rho_r = 2$; the flow velocity is $u_m = 2.72$. First, the sphere is fixed in the tube with a horizontal deviation of $1.09d$ (the equilibrium position of the freely moving sphere in Poiseuille flow) in the positive y-direction, as shown in Fig. 14. Then, the rotation of the sphere is permitted. When the sphere motion is fully developed, the restrictions on the translational DOFs of the sphere motion are removed. The hydrodynamic forces, the sphere velocity and the equilibrium position are shown in Figs. 15–17, respectively.

First, the sphere is fixed in Poiseuille flow. The drag and lift forces are constant in the fully developed state, as shown in Fig. 15(a). It is noted that the lift force points toward the tube wall ($F_y > 0$), indicating that the sphere would move toward the wall once the sphere is released; the moment ($M_x > 0$) tends to make the sphere rotate in the positive x-direction (the counterclockwise direction), as shown in Fig. 15(b). As mentioned in Section 4.1.1, the large Re_s contributes significantly to the lift force. This is reflected by the asymmetric flow field and a steady lift force on the sphere when the sphere is exposed to the homogeneous flow at the same Reynolds number (Johnson and Patel, 1999). As the sphere is fixed in Poiseuille flow, the flow velocity on the left side of the sphere (near the tube center, see Fig. 14) is larger than that on the right
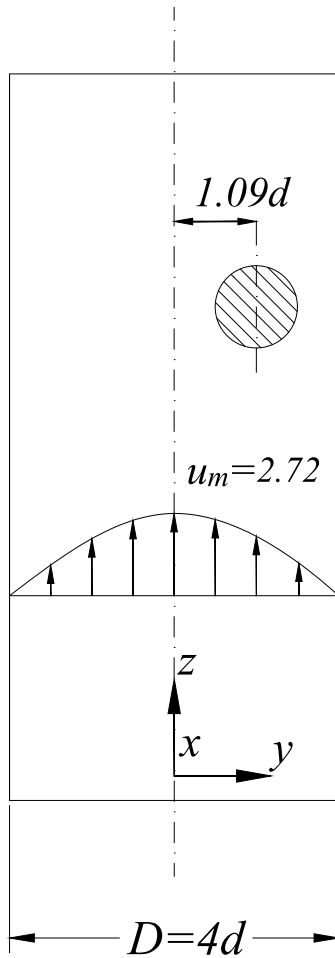
Fig. 14. Configuration of the constrained simulations.

side (near the wall), indicating the lower pressure on the left side. Therefore, the shear of Poiseuille flow has the tendency to impel the sphere to the tube center. This tendency will not change when the sphere is released, due to the large slip velocity of the "heavy" sphere (Feng et al., 1994). Additionally, the flow on the right side of the sphere is affected by the wall; the wall-wake interaction gives rise to the repulsive effect on the sphere (Feng et al., 1994). The effects of Re_s, the shear and the wall reach a stable state, producing a resultant lift force towards the tube wall.

Once the rotational DOFs are permitted, the unbalanced M_x makes the sphere rotate in the counterclockwise direction ($\omega_x > 0$, see Fig. 16(b)). Both drag and lift forces increase owing to the sphere

rotation. It is noteworthy that the increase of the lift force F_y is significant and mainly caused by the pressure difference on the sphere surface; the contribution of the shear stress is negligible, as shown in Fig. 18. An explanation for the increase of F_y is the Magnus effect, which is related to the angular velocity ω_x and slip velocity V_{slip}. The counterclockwise rotation of the sphere accelerates the fluid on the right (near the wall) and slows the fluid on the left (near the tube), creating an additional pressure difference and increasing the lift force toward the tube wall. The Magnus effect was considered to be small or negligible for neutrally and slightly non-neutrally buoyant spheres in upward Poiseuille flow owing to the small density ratio and the corresponding Re_s (Feng et al., 1994; Yu et al., 2004). As Re_s increases to $Re_s \approx O(10^2)$, the Magnus force will play an essential role in the horizontal migration of the freely moving sphere in Poiseuille flow.

Finally, the translational DOFs are unlimited and the sphere moves freely in Poiseuille flow. Once the sphere is released, it accelerates in the vertical direction owing to the drag force F_z and attains a constant vertical velocity V_z finally, as shown in Fig. 16(a). In the radial direction, the sphere moves toward the wall owing to the unbalanced lift force F_y. However, it is immediately exposed to the repulsive wake-wall interaction, which tends to push the sphere away from the wall. Meanwhile, a negative M_x appears (see Fig. 15(b)) and suppresses the sphere rotation (Fig. 16(b)). The Magnus effect is weakened owing to the decrease of both ω_x and the relative velocity between the sphere and the fluid. Therefore, the sphere decelerates rapidly and moves toward the tube center subsequently. The wall repulsion decreases as the increase of the gap between the sphere and the wall. A positive M_x is introduced and impels the sphere to rotate counterclockwise. The Magnus effect is recovered gradually. The sphere decelerates and then moves toward the wall again. After several oscillations, the effects of the wall, the shear, the sphere rotation and Re_s achieve a balance; the sphere reaches a radial equilibrium position.

In summary, the final states of a "heavy" sphere in Poiseuille flow is determined by the combined effects of Re_s, the shear of Poiseuille flow, the sphere rotation and the wall. The large slip Reynolds number Re_s owing to the large density ratio ρ_r makes significant contributions to the lift force. The shear of Poiseuille flow tends to push the sphere toward the tube center. The Magnus effect due to the sphere rotation is significant at $Re_s \approx O(10^2)$ and tends to impel the sphere toward the tube wall. The repulsive wall-wake interaction affects the lift force strongly and pushes the sphere away from the wall. Additionally, the wall has a tendency to suppress the sphere rotation and diminish the Magnus effect.

4.3. Role of density ratio

The density ratio ρ_r plays an important role in the sphere motion in Poiseuille flow. As the density ratio increases, the slip Reynolds number $Re_s = V_{slip}d/\nu$ changes, resulting in different flow field around the
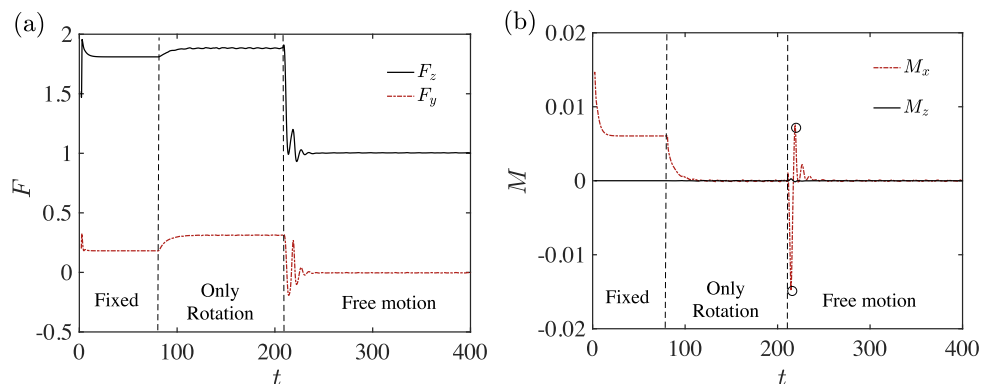

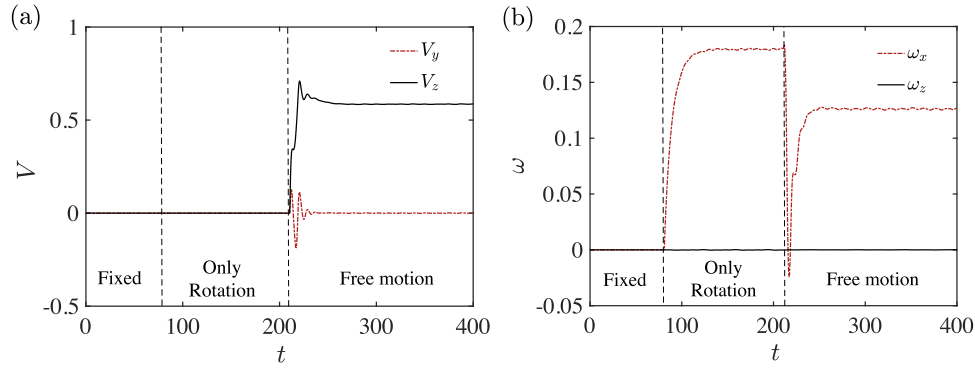**Fig. 15.** Hydrodynamic (a) forces and (b) moments on sphere.

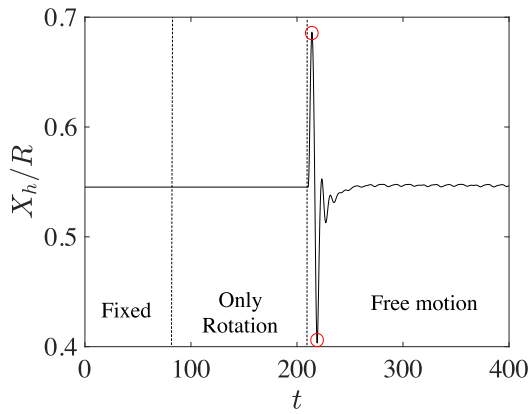**Fig. 16.** (a) Velocity and (b) angular velocity of sphere.
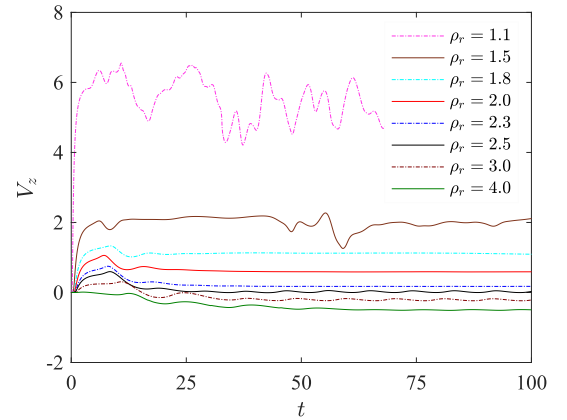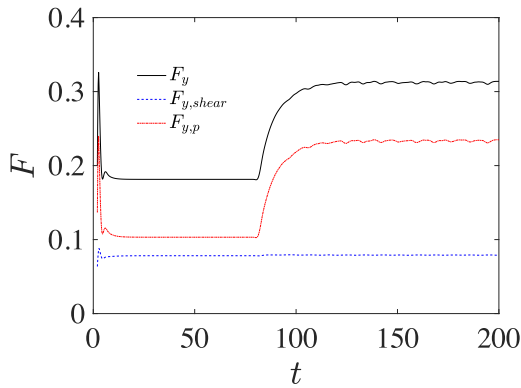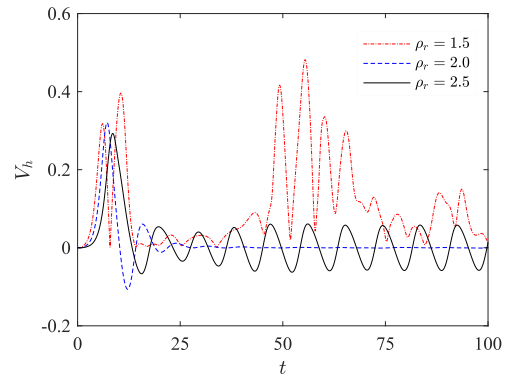

Fig. 17. Radial equilibrium position of sphere.

Fig. 19. Vertical velocity of sphere at different density ratios ρ_r.

Fig. 18. Shear ($F_{y,shear}$) and pressure ($F_{y,p}$) components of lift force.

Fig. 20. Horizontal velocity of sphere at different density ratios ρ_r.

sphere. The contributions of the shear, the wall, the sphere rotation and Re_s to the final state of the sphere will be altered. In this section, the sphere motion and the flow field in Poiseuille flow are simulated at $1.1 \leq \rho_r \leq 4.0$. Without loss of generality, the tube Reynolds number $Re_t = 1106$ ($u_m = 2.72$) is selected.

The calculated vertical velocity V_z, horizontal velocity V_h, and angular velocity ω_h of the sphere are presented in Figs. 19–21, respectively. Owing to the difficulty to measure the directions of V_h and ω_h in the chaotic state, the magnitudes of V_h and ω_h at $\rho_r = 1.5$ are provided as an alternative in Figs. 20 and 21. The fully developed wake structures at different ρ_r are shown in Fig. 22. In general, three types of path trajectories of the sphere are observed at $Re_t = 1106$: steady, periodic oscillating, and chaotic.

When the density ratio is small ($\rho_r = 1.1$ and 1.5), the path

trajectory of the sphere is chaotic. The vertical velocity V_z varies randomly within a certain range (Fig. 19). The horizontal and angular velocities are irregular (Figs. 20 and 21). The wake structures around the sphere are disordered as shown in Fig. 22(a). The slip Reynolds number at $\rho_r = 1.5$ is approximate 220. The lift introduced by Re_s is much smaller and has a weaker effect on the sphere when compared to the case of $\rho_r = 2$, $Re_s = 263$ (Johnson and Patel, 1999). Due to the small inertia of the sphere at $\rho_r = 1.5$, the sphere motion will be affected by any small perturbations. Once the sphere is released, it moves away from the tube center and oscillates in the flow. The oscillations of the released sphere disrupt the flow in the tube; the lift related to the shear becomes chaotic and will never be balanced by the effects of Re_s, the sphere rotation and the wall. The flow and the sphere motion will never obtain stable states.

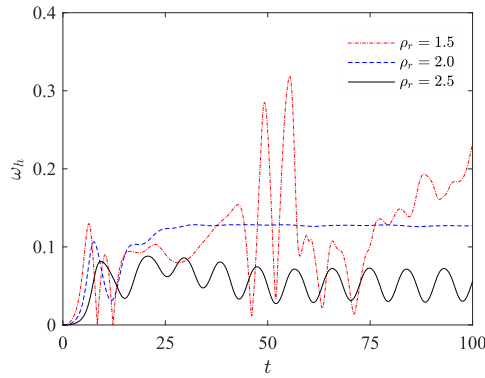As the density ratio increases ($\rho_r = 1.8$, 2.0, and 2.3), the sphere

Fig. 21. Angular velocity of sphere at different density ratios ρ_r.

(a) $\rho_r = 1.5$ (b) $\rho_r = 2.0$ (c) $\rho_r = 2.5$

Fig. 22. Wake structures of flow (identified by the iso-surfaces of Q) at different density ratios ρ_r.

moves vertically in a radial equilibrium position (see Figs. 19 and 20) and rotates at a constant angular velocity (see Fig. 21) in the final state. Fig. 22(b) reveals the constant wake structures which have been described in Section 4.1.1. The equilibrium state is related to the larger inertia of the sphere and the effect of a larger Re_s which overwhelms the lift caused by the shear. Finally, the effects of all the factors attain the balance, leading to stable states of the sphere and the flow field.

At $\rho_r = 2.5$, 3.0 and 4.0, the periodic oscillations of the sphere velocity, including V_z, V_h, and ω_h, are observed in Figs. 19–21. The vortex shedding behind the sphere is revealed in Fig. 22(c). The average slip Reynolds number at $\rho_r = 2.5$ is $Re_s = 320$, at which the periodic vortex shedding appears behind the sphere in the case of flow past a sphere (Johnson and Patel, 1999). It is reasonable to believe that the effect of Re_s plays a dominating role in the lift force, thereby resulting in the periodic oscillations of the sphere, although the frequency of the vortex

shedding is different from that of flow past a fixed sphere.

5. Concluding remarks

A "heavy" sphere moving in upward Poiseuille flow is numerically investigated using DNS method. The overset mesh and the moving computation domain are utilized to address the long-distance motion of the sphere. We mainly focus on the dynamic responses of the sphere, including the path trajectory, the slip velocity and the radial equilibrium position in the tube. The flow patterns and the hydrodynamic forces are revealed. The effect of the tube Reynolds number Re_t on the "heavy" sphere ($\rho_r = 2$) is evaluated with Re_t up to 1998. A wide range of density ratio $1.1 \leq \rho_r \leq 4$ is selected to investigate the role of density on sphere migration in Poiseuille flow; the corresponding slip Reynolds number is $Re_s \approx O(10^2)$. The results are likely to provide potential guidance on selecting the flow velocity to transport the "heavy" particles in vertical pipes. The main conclusions are drawn as follows:

1. Dependent on the tube Reynolds number, five types of path trajectories of the "heavy" sphere ($\rho_r = 2$) are observed: helical falling, oscillating falling, vertical falling, vertical rising, and chaotic rising.
2. The slip velocity changes marginally with tube Reynolds number Re_t at a constant ρ_r. The sphere will be lifted when the flow velocity u_m is larger than a critical value. The radial equilibrium position of the sphere at $\rho_r \approx 2$ varies in a wide range of $0.4 \leq X_h/R \leq 0.66$. The largest X_h/R corresponds to the suspending state of a sphere in Poiseuille flow.
3. Different from the neutrally and slightly non-neutrally buoyant spheres, a "heavy" sphere gives rise to a much larger slip Reynolds number Re_s, which effects the lift force and the final state of sphere motion significantly. The lift force associated with the rotation of a "heavy" sphere is much larger than that in the cases of neutrally and slightly non-neutrally buoyant spheres. The shear tends to push the sphere toward the tube center. The wall repulsion contributes substantially to the horizontal migration of the sphere and exhibits the tendency to suppress the sphere rotation. The final states of the sphere are affected by the slip Reynolds number Re_s, the shear of Poiseuille flow, the sphere rotation and the wall repulsion.
4. The density ratio plays a significant role in the dynamic responses of a "heavy" sphere in Poiseuille flow. With the variation of ρ_r ($1.1 \leq \rho_r \leq 4$), three types of path trajectories are observed at $Re_t = 1106$: steady, periodic oscillating, and chaotic.

References

Asao, S., Matsuno, K., Yamakawa, M., 2013. Parallel computations of incompressible flow around falling spheres in a long pipe using moving computational domain method. Comput. Fluids 88, 850–856.

Asmolv, E.S., 1999. The inertial lift on a spherical particle in a plane Poiseuille flow at large channel Reynolds number. J. Fluid Mech. 381, 6387.

Brenner, H., 1966. Hydrodynamic resistance of particles at small Reynolds numbers. Adv. Chem. Eng. 6 287–438.

Bretherton, F.P., 1962. The motion of rigid particles in a shear flow at low Reynolds number. J. Fluid Mech. 14, 284304.

CD-adapco, 2016. User Guide, STAR-CCM+. Version 11, 06 ed. CD-adapco.

Chandar, D.D., Boppana, B., Kumar, V., 2018. A comparative study of different overset grid solvers between OpenFOAM, StarCCM+ and ansys-fluent. In: AIAA Aerospace Sciences Meeting. American Institute of Aeronautics and Astronautics, Reston, Virginia, pp. 22 2018.

Clift, R., Grace, J.R., Weber, M.E., 1978. Bubbles, Drops, and Particles. Academic Press.

Cox, R.G., Mason, S.G., 1971. Suspended particles in fluid flow through tubes. Annu. Rev. Fluid Mech. 3, 291–316.

Deloze, T., Hoarau, Y., Duek, J., 2012. Transition scenario of a sphere freely falling in a

vertical tube. J. Fluid Mech. 711, 40–60.

Feng, J., Hu, H.H., Joseph, D.D., 1994. Direct simulation of initial value problems for the motion of solid bodies in a Newtonian fluid. part 2. Couette and Poiseuille flows. J. Fluid Mech. 277, 271–301.

Hadzic, H., 2006. Development and Application of Finite Volume Method for the Computation of Flows Around Moving Bodies on Unstructured, Overlapping Grids (Thesis). .

Hogg, A.J., 1994. The inertial migration of non-neutrally buoyant spherical particles in two-dimensional shear flows. J. Fluid Mech. 272, 285–318.

Horowitz, M., Williamson, C.H.K., 2010. The effect of Reynolds number on the dynamics and wakes of freely rising and falling spheres. J. Fluid Mech. 651, 251–294.

Hunt, J., Wray, A., Moin, P., 1988. Eddies, Streams, and Convergence Zones in Turbulent Flows. Center for Turbulence Research Report CTR-S88, pp. 193–208.

Jeffrey, R.C., Pearson, J.R.A., 1965. Particle motion in laminar vertical tube flow. J. Fluid Mech. 22, 721–735.

Jenny, M., Dušek, J., Bouchet, G., 2004. Instabilities and transition of a sphere falling or ascending freely in a Newtonian fluid. J. Fluid Mech. 508, 201–239.

Jiang, R., Lin, J., Chen, Z., 2013. Vibrations of cylindrical objects obstructing a Poiseuille-type flow. Phys. Rev. E 88, 023009.

Johnson, T.A., Patel, V.C., 1999. Flow past a sphere up to a Reynolds number of 300. J. Fluid Mech. 378, 1970.

Karnis, A., Goldsmith, H., Mason, S., 1966. The flow of suspensions through tubes: V. inertial effects. Can. J. Chem. Eng. 44, 181–193.

Koblitz, A.R., Lovett, S., Nikiforakis, N., Henshaw, W.D., 2017. Direct numerical simulation of particulate flows with an overset grid method. J. Comput. Phys. 343, 414–431.

Leal, L.G., 1980. Particle motions in a viscous fluid. Annu. Rev. Fluid Mech. 12, 435–476.

Liang, Y., Tao, L., 2017. Interaction of vortex shedding processes on flow over a deep-draft semi-submersible. Ocean Eng. 141, 427–449.

Liu, M., Xiao, L., Yang, J., Tian, X., 2017. Parametric study on the vortex-induced motions of semi-submersibles: effect of rounded ratios of the column and pontoon. Phys. Fluids 29, 055101.

Matas, J.P., Morris, J.F., Guazzelli, É., 2003. Transition to turbulence in particulate pipe flow. Phys. Rev. Lett. 90, 014–501.

Matas, J.P., Morris, J.F., Guazzelli, É., 2004a. Inertial migration of rigid spherical particles in Poiseuille flow. J. Fluid Mech. 515, 171–195.

Matas, J.P., Morris, J.F., Guazzelli, É., 2004b. Lateral forces on a sphere. Oil & Gas Science and Technology - Rev. IFP 59, 59–70.

Namkoong, K.A.K., Yoo, J.Y., Choi, H.G., 2008. Numerical analysis of two-dimensional motion of a freely falling circular cylinder in an infinite fluid. J. Fluid Mech. 604, 33–53.

Patankar, N.A., Huang, P.Y., Ko, T., Joseph, D.D., 2001. Lift-off of a single particle in Newtonian and viscoelastic fluids by direct numerical simulation. J. Fluid Mech. 438, 67–100.

Rahmani, M., Wachs, A., 2014. Free falling and rising of spherical and angular particles. Phys. Fluids 26, 083301.

Romero-Gomez, P., Richmond, M.C., 2016. Numerical simulation of circular cylinders in free-fall. J. Fluid Struct. 61, 154–167.

Saffman, P.G., 1965. The lift on a small sphere in a slow shear flow. J. Fluid Mech. 22, 385–400.

Schonberg, J.A., Hinch, E.J., 1989. Inertial migration of a sphere in Poiseuille flow. J. Fluid Mech. 203, 517524.

Segré, G., Silberberg, A., 1961. Radial particle displacements in Poiseuille flow of suspensions. Nature 189, 209–210.

Shao, X., Yu, Z., Sun, B., 2008. Inertial migration of spherical particles in circular Poiseuille flow at moderately high Reynolds numbers. Phys. Fluids 20, 103307.

Tian, X., Hu, Z., Lu, H., Yang, J., 2017a. Direct numerical simulations on the flow past an inclined circular disk. J. Fluid Struct. 72, 152–168.

Tian, X., Xiao, L., Zhang, X., Yang, J., Tao, L., Yang, D., 2017b. Flow around an oscillating circular disk at low to moderate Reynolds numbers. J. Fluid Mech. 812, 1119–1145.

Yang, B.H., Wang, J., Joseph, D.D., Hu, H.H., Pan, T.W., Glowinski, R., 2005. Migration of a sphere in tube flow. J. Fluid Mech. 540, 109131.

Yu, Z., Phan-Thien, N., Tanner, R.I., 2004. Dynamic simulation of sphere motion in a vertical tube. J. Fluid Mech. 518, 61–93.

Zhou, W., Dušek, J., 2015. Chaotic states and order in the chaos of the paths of freely falling and ascending spheres. Int. J. Multiphas. Flow 75, 205–223.